1

Selecting appropriate model complexity: An example of tracer inversion for thermal prediction in enhanced geothermal systems

4

Hui Wu[1,2], Zhijun Jin[1,2,3], Su Jiang[4], Hewei Tang[5], Joseph P. Morris[5], Jinjiang Zhang[1], Bo Zhang[1]

[1] School of Earth and Space Sciences, Peking University, Beijing, China.

[2] Institute of Energy, Peking University, Beijing, China.

[3] Petroleum Exploration and Production Research Institute, SINOPEC, Beijing, 100083, China

[4] Department of Energy Resources Engineering, Stanford University, Stanford, CA, USA.

[5] Lawrence Livermore National Laboratory, Livermore, CA, USA.

Corresponding author: Hui Wu (hui.wu@pku.edu.cn)

Key Points:

- Combined dimensionality reduction and data assimilation to infer fracture aperture distribution from tracer recovery data.

- Quantitatively investigated the effect of model complexities on the aperture inversion and thermal prediction of a field-scale EGS.

- A moderate model complexity is sufficient to reproduce tracer recovery data and provide accurate thermal predictions.

Abstract

A major challenge in the inversion of subsurface parameters is the ill-posedness issue caused by the inherent subsurface complexities and the generally spatially sparse data. Appropriate simplifications of inversion models are thus necessary to make the inversion process tractable and meanwhile preserve the predictive ability of the inversion results. In the present study, we investigate the effect of model complexity on the inversion of fracture aperture distribution as well as the prediction of long-term thermal performance in a field-scale single-fracture EGS model. Principal component analysis (PCA) was used to map the original cell-based aperture field to a low-dimensional latent space. The complexity of the inversion model was quantitatively represented by the percentage of total variance in the original aperture fields preserved by the latent space. Tracer, pressure and flow rate data were used to invert for fracture aperture through an ensemble-based inversion method, and the inferred aperture field was then used to predict thermal performance. We found that an over-simplified aperture model could not reproduce the inversion data and the predicted thermal response was biased. A complex aperture model could reproduce the data but the thermal prediction showed significant uncertainty. A model with moderate complexity, although not resolving many fine features in the "true" aperture field, successfully matched the data and predicted the long-term thermal behavior. The results provide important insights into the selection of model complexity for effective subsurface reservoir inversion and prediction.

1 Introduction

Flow and transport processes in geothermal reservoirs highly depend on spatially heterogeneous reservoir properties, such as permeability distribution in a hydrothermal system (Cox et al., 2001; Dobson et al., 2003; Shi et al., 2018) and fracture aperture distribution in an enhanced geothermal system (EGS) (Chen & Zhao, 2020; Guo, Fu, Hao, Peters, & Carrigan, 2016; Okoroafor et al., 2022; Wu, Fu, Morris, et al., 2021). Characterizing permeability/aperture fields is important for the modeling, prediction, optimization and long-term risk management of geothermal reservoirs. However, due to the high cost and technical difficulties in directly measuring subsurface fields, available permeability/aperture data are generally spatially sparse. A comprehensive characterization is often performed through the inversion of indirect hydraulic or geophysical data, such as hydraulic and tracer testing data (Berkowitz, 2002; Chen et al., 2013; Somogyvári et al., 2017; Vogt et al., 2012; Wu, Fu, Hawkins, et al., 2021), electrical resistivity (Johnson et al., 2021; Wu et al., 2019), seismic (Emerick, 2018; Liu & Grana, 2020), and so on. A key component of hydraulic/geophysical inversion is a reliable model that can properly simulate the underlying physical processes and output model responses for given model parameters. As analytical models are only applicable to idealized scenarios with over simplified fields, numerical models are required for the inversion of representative fields in real-world applications. The infinite-dimensional space of a heterogeneously distributed field is projected to a finite-dimensional parameter space by discretizing the model on a finite element mesh.

A major challenge in permeability and aperture inversion is the ill-posedness issue caused by the high dimensionality of model parameter space and the scarcity of hydraulic/geophysical data. A reliable numerical approximation of model responses requires a relatively fine discretization, which inevitably leads to a high-dimensional parameter space. Practically available hydraulic/geophysical data are usually insufficient to constrain such a high-dimensional parameter space. To tackle this challenge, dimensionality reduction methods have been used to

65   map the discretization-dependent, cell-based high-dimensional parameter space to a low-
66   dimensional latent space (Jiang et al., 2021; Laloy et al., 2013; Marzouk & Najm, 2009; Tang et
67   al., 2021; Xiao et al., 2022; Zhu & Zabaras, 2018). Principal component analysis (PCA) is a
68   conventional dimensionality reduction method, which learns spatial similarities in training
69   samples (prior permeability or aperture models) and compress the most salient features into a
70   latent space defined by orthogonal principal components (Hawkins et al., 2020; Sarma et al.,
71   2008; Wu, Fu, Hawkins, et al., 2021; Zhang et al., 2020). As a linear transform method, PCA is
72   applicable to Gaussian and log-normal fields that can be fully characterized by two-point
73   statistics. For fields that follow non-Gaussian distributions, nonlinear transform methods are
74   required for effective dimensionality reduction, such as deep learning-based methods (e.g.,
75   generative adversarial network and variational autoencoder) that have been widely explored in
76   the recent literature (Canchumuni et al., 2020; Jiang & Jafarpour, 2021; Laloy et al., 2018; Mo et
77   al., 2020).

78   The reduction of model dimensionality essentially leads to the reduction of model
79   complexity. In a cell-based parameter space, each cell value is tuned independently during
80   inversion, and the model has the maximum variance. Through dimensionality reduction, the prior
81   knowledge in training samples, such as spatial auto-correlation and statistical features, are
82   learned and used to reduce the model degree of freedom (model complexity). The learned prior
83   knowledge serves to constrain the heterogeneous distribution of permeability/aperture fields and
84   regularize subsequent inversion. Inversion on a low-dimensional latent space not only mitigates
85   the ill-posedness issue and make the inversion computationally tractable, but also better honors
86   the spatial auto-correlation nature of permeability/aperture fields than inversion on a cell-based
87   parameter space does. The tuning of a latent parameter changes the overall spatial distribution of
88   a field rather than its value at a single cell, which is a highly desired feature for inversion in a
89   data-scarce environment.

90   Latent space dimensionality, as a quantitative measure of model complexity, is a
91   hyperparameter that needs to be carefully determined prior to dimensionality reduction. On the
92   one hand, model complexity should be deliberately compromised to accommodate the limited
93   information in hydraulic/geophysical data. On the other hand, the model needs to capture
94   adequate variations in the unknown field to appropriately simulate the underlying physical
95   processes. An extremely complex model is prone to overfitting and may undermine the
96   predictive ability of the inferred permeability/aperture fields, while an over-simplified model
97   may fall into the opposite error of underfitting and be unable to reproduce hydraulic/geophysical
98   data. Unfortunately, due to the many inherent complexities of subsurface reservoirs, it is
99   difficult, if not impossible, to predetermine an ideal model complexity for permeability/aperture
100   inversion from hydraulic/geophysical data. In most previous studies, the dimensionality of latent
101   space is subjectively determined (Yang et al., 2021). Some studies used relatively large latent
102   spaces to preserve at least 90% of the total variance in original cell-based parameter spaces when
103   using PCA for dimensionality reduction (Hawkins et al., 2020; Laloy et al., 2013; Tang et al.,
104   2021; Zhao & Luo, 2020). Some other studies, on the other hand, preserved $50\% \sim 60\%$ of the
105   total variance through relatively small latent spaces (Romary, 2009; Fernández-Martínez et al.,
106   2012; Emerick, 2017). The dimensionality of the resultant latent spaces in these studies varies
107   from 30 to 1,000.

108   Although dimensionality reduction methods have been widely used in
109   permeability/aperture inversion, how to select an appropriate model complexity/latent space to

110   circumvent the dilemma of overfitting and underfitting remains unclear. The effects of model
111   complexity on permeability/aperture inversion and subsequent reservoir performance prediction
112   require further investigation. Several studies examined the effect of latent space dimensionality
113   on forward simulation accuracy by first generating permeability/facies fields from latent spaces
114   with different dimensionalities, and then performing forward simulations on these generated
115   fields (Romary, 2009; Fernández-Martínez et al., 2012). The results indicated that a small latent
116   space (preserving 50% - 60% of the total variance in the original cell-based parameter spaces)
117   was sufficient to accurately simulate the underlying physical processes. Li & Cirpka (2006)
118   investigated the effect of latent space dimensionality on the inversion of a 2D hydraulic
119   conductivity field. With the increase of latent space dimensionality, the consumed computational
120   resources increased, while the inversion error (defined as the root mean square error between
121   true and inferred fields) gradually decreased and converged to a stable value. These studies focus
122   on the effect of model complexity on forward and inversion modeling, but lack analysis of the
123   predictive ability of the inversion results. Results from these studies provide insights into the
124   lower limit of model complexity to prevent underfitting. However, the upper limit of model
125   complexity to avoid overfitting, which manifests as good data match but poor predictive ability,
126   remains unexplored.

127   The main goal of the present study is to investigate the effect of model complexity on the
128   inversion of fracture aperture distribution as well as the prediction of long-term thermal recovery
129   in an EGS. PCA is used to map the original cell-based aperture distribution to a latent space. The
130   corresponding model complexity is quantitatively represented by the percentage of total variance
131   in the original aperture fields preserved by the latent space. An ensemble-based inversion
132   method, ensemble smoother with multiple data assimilation (ES-MDA), is used for aperture
133   inversion from practically available tracer, pressure and flow rate data. Through this
134   investigation, we aim to analyze not only the minimum model complexity required to
135   appropriately reproduce tracer/pressure/flow rate data, but also the impact of overfitting on
136   thermal performance prediction due to excessive model complexity. The paper is organized as
137   follows. In Section 2, we introduce PCA for the dimensionality reduction of spatially auto-
138   correlated aperture fields. Aperture fields generated from latent spaces with different
139   dimensionalities are compared to demonstrate the effect of latent space dimensionality on model
140   complexity. Section 3 describes a field-scale synthetic EGS model with a predominant horizontal
141   fracture, followed by the introduction of forward simulation methods (flow, tracer and thermal)
142   as well as a data assimilation framework using ES-MDA. In Section 4, synthetic tracer, pressure
143   and flow rate data are provided to ES-MDA to invert for the latent space obtained from PCA.
144   The inverted latent space is then mapped back to a cell-based aperture field to predict the thermal
145   performance of the EGS model. A series of latent spaces with different dimensionalities are
146   analyzed to investigate the effect of model complexity. Section 5 provides discussions regarding
147   the implication of the results.

148   **2 Principal component analysis for dimensionality reduction**

149   Principle component analysis (PCA), also known as Karhunen-Loève (KL) expansion, is
150   a well-established dimensionality reduction method. It has been broadly used in many subsurface
151   inversion problems to map Gaussian or log-normal fields (e.g., permeability and aperture) to
152   low-dimensional latent spaces that follow the standard normal distribution (Hawkins et al., 2020;
153   Wu, Fu, Hawkins, et al., 2021). To perform PCA on the field of interest, we first generate an
154   ensemble of training fields based on our prior knowledge of the field obtained from

155   geological/geophysical investigations such as core logs, wellbore images and outcrop analysis.
156   The reduction of dimensionality is then achieved by first computing orthogonal principal
157   components from the training fields, and then retaining the most significant principal
158   components as the basis functions to generate new fields through linear combination. The
159   principal components can be calculated through either computing the eigenvectors and
160   eigenvalues of the covariance matrix of the training fields, or directly performing singular value
161   decomposition (SVD) on the training fields. The significance of a principal component is
162   represented by the percentage of the total variance in the training fields preserved by the
163   principal component. For a spatially auto-correlated field, most of the variance in the training
164   fields can be effectively preserved by a small number of principal components. New fields
165   generated from the linear combination of the retained principal components have the same
166   dimensionality as the training fields, and are fully controlled by the weights of the retained
167   principal components. These weights form the latent space to be inferred in subsequent
168   inversion. The detailed procedure of PCA has been widely reported in the literature (Liu &
169   Durlofsky, 2020; Wu, Fu, Hawkins, et al., 2021) and therefore not repeated here.

170   In the current study, the field of interest is the aperture distribution of a 2D fracture. To
171   demonstrate the relationship between latent space dimensionality (i.e., the number of retained
172   principal components) and model complexity, we perform PCA on training aperture fields and
173   then compare the aperture fields reconstructed/generated with different numbers of principal
174   components. We generate 5,000 aperture fields on an 800 m × 800 m domain discretized into a
175   160 × 160 regular grid. We use sequential gaussian simulations and assume a spherical
176   variogram with a mean of 0.6 mm, a standard deviation of 0.45 mm and a correlation length of
177   75 m. The generated aperture fields follow a log-normal distribution, and are provided to PCA as
178   training fields. After PCA, 5,000 principal components are obtained and ranked in a descending
179   order according to their significance, i.e., percentage of preserved variance. We then use the first
180   l principal components to reconstruct training aperture fields as well as generate new aperture
181   fields.

182   We first analyze the effect of l on training aperture field reconstruction. A random
183   aperture field is selected from the training ensemble and reconstructed with $l = 2, 10, 50, 200$ and
184   800 as shown in Fig. 1. The preserved percentage of total variance is 1%, 5%, 21%, 56% and
185   84% for $l = 2, 10, 50, 200$ and 800 respectively. With a small l, the reconstructed aperture field is
186   almost uniform and misses most of the variance in the training aperture field. With the increase
187   of l, the complexity of the reconstructed aperture field increases, manifesting as the capture of
188   fine features in the training aperture field.

189   We then analyze the effect of l on new aperture field generation. A random l-dimensional
190   latent parameter vector is first sampled from the standard normal distribution, and then used as
191   the weights of the retained l principal components to generate a new aperture field. For each l,
192   we generated 30 aperture fields and analyze their mean, standard deviation and correlation length
193   (Fig. 2). The new aperture fields also follow log-normal distributions, but the mean, standard
194   deviation and correlation length are different from that of the training fields. Compared with the
195   training aperture fields, aperture fields generated from latent spaces exhibit smaller mean and
196   standard deviation, and larger correlation length. For an extremely small latent space ($l = 2$), the
197   mean of the generated aperture fields is slightly smaller than that of the training aperture fields.
198   The standard deviation is significantly smaller than that of the training aperture fields, and the
199   correlation length shows the opposite trend. A smaller standard deviation and a larger correlation

length lead to a smoother aperture distribution, and therefore a less complex aperture model. With the increase of l, the mean, standard deviation and correlation length gradually approaches to their corresponding values in the training aperture fields.
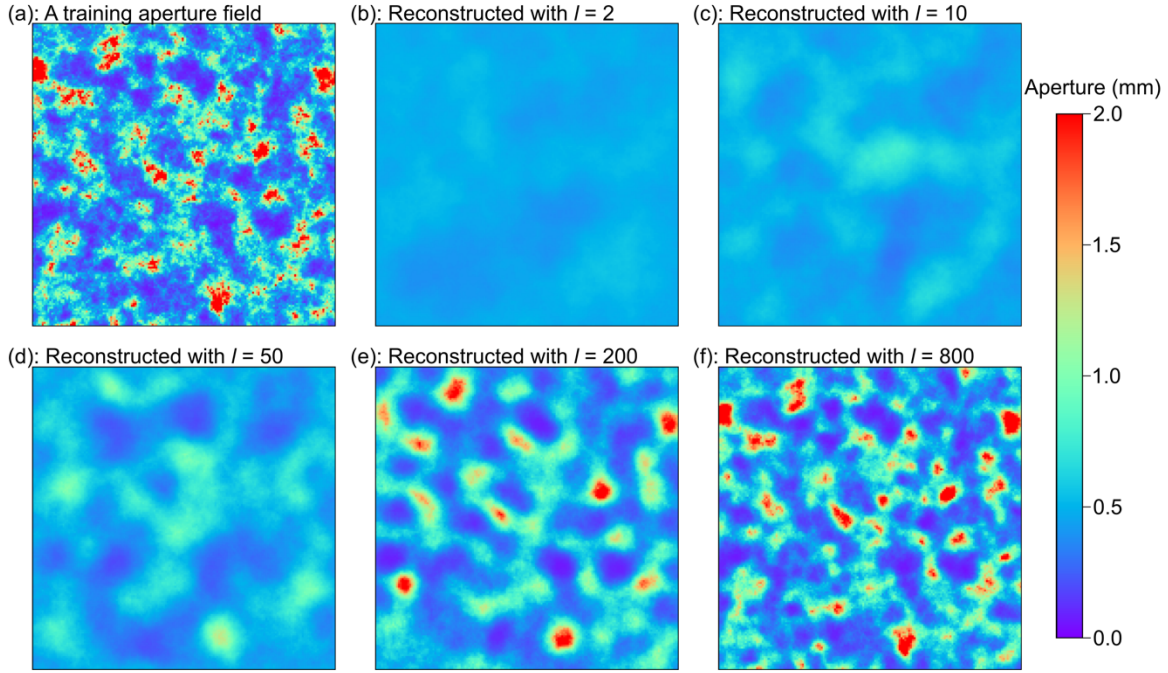

Fig. 1 Reconstruction of a training aperture field. (a) A randomly selected aperture field from the training ensemble. (b) ~ (f) Reconstructed aperture fields using different numbers of principal components.
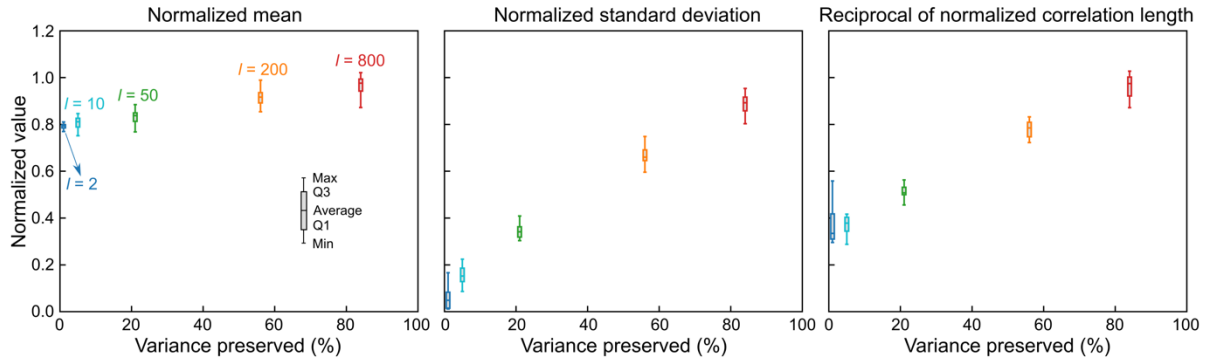

Fig. 2 Box plots of mean, standard deviation and correlation length of aperture fields generated with different numbers of principal components. The box plots show the minimum, maximum, average, as well as the 25% (Q1) and 75% (Q3) percentiles. The mean, standard deviation and correlation length are normalized by their corresponding values used to generate the training aperture fields, i.e., 0.6 mm, 0.45 mm and 75 m respectively. For correlation length, we show the reciprocal of the normalized correlation length.

3 An EGS model and forward simulation/inversion methods

In this section, we develop a field-scale single-fracture EGS model to demonstrate the effect of model complexity on aperture inversion and thermal prediction (Fig. 3). Data used for aperture inversion include practically available tracer, pressure and flow rate data. In what

218   follows, we first describe the model details and then the numerical simulation of flow, tracer
219   transport and thermal extraction in the EGS model. Finally, we briefly introduce a data
220   assimilation framework developed in our previous work (Wu, Fu, Hawkins, et al., 2021), which
221   has proven an effective method for aperture inversion and thermal prediction.

222   3.1 A field-scale single-fracture EGS model

223   The developed EGS model is $3000 \times 3000 \times 3000$ m^3 in dimension with a horizontal
224   circular fracture 800 m in diameter, located at the center of the model. An injection well and two
225   production wells are connected by the fracture (Fig. 3(a)). A vertical temperature gradient of
226   40 °C/km is assumed in the model with an initial temperature of 200 °C at the fracture depth.
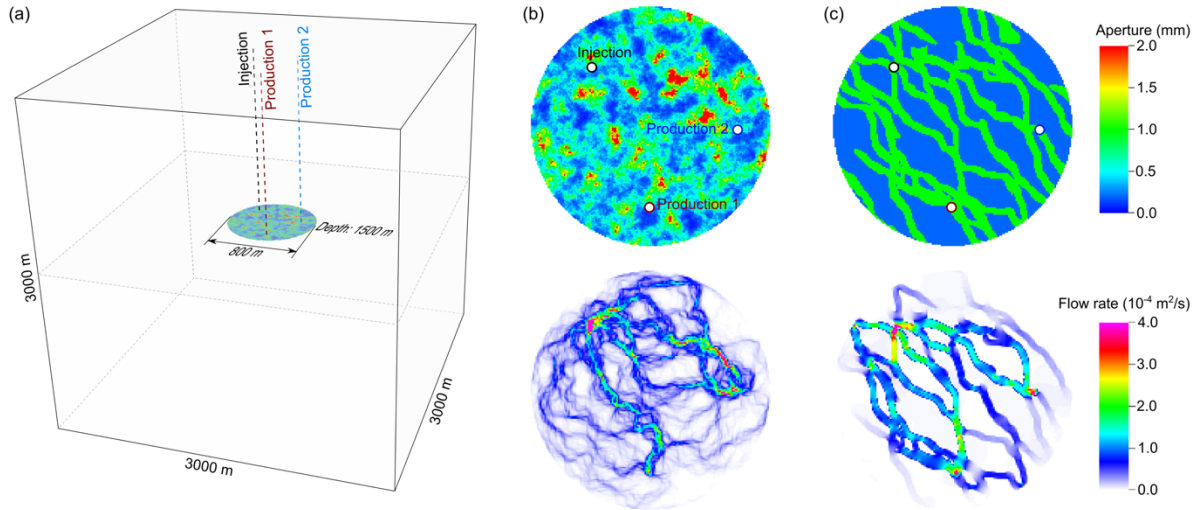

227
228   Fig. 3 (a) A field-scale EGS model with a horizontal circular fracture located at 1,500 m depth.
229   (b) A Gaussian aperture field and the corresponding flow field under 20 L/s injection rate and
230   constant pressure at the two production wells. (c) A non-Gaussian, two facies aperture field and
231   the corresponding flow field under 20 L/s injection rate and constant pressure at the two
232   production wells.

233   We investigate two "true" aperture fields, one is a spatially auto-correlated log-normal
234   field (Fig. 3(b)) and the other is a two facies field (Fig. 3(c)). The log-normal aperture field is
235   randomly generated from sequential gaussian simulation assuming a spherical variogram with a
236   mean of 0.6 mm, a standard deviation of 0.45 mm and a correlation length of 75 m. The two
237   facies aperture field is generated using the 'snesim' geostatistical algorithm (Strebelle, 2002)
238   from a geostatistical tool box SGeMS (Remy et al., 2009). The background aperture is 0.2 mm
239   and the aperture of flow channels is 1 mm. Note that the three wells are connected by flow
240   channels. Although the two aperture fields follow different statistical distributions, we use the
241   same aperture model in subsequent inversion for them, i.e., log-normal aperture model. We use
242   the two facies aperture example to demonstrate the scenario where the statistical distribution of
243   the ground truth field fundamentally differs from that of the assumed aperture distribution in the
244   inversion process. This is commonly encountered in real-world problems as the ground truth
245   field is complex and we do not have sufficient data to correctly characterize its statistical
246   distribution.

247   3.2 Flow, tracer and thermal simulation

248   Flow and tracer simulation is performed to generate synthetic data for the "true" aperture
249 fields, including tracer breakthrough curves (BTCs) and flow rates at the two production wells,
250 as well as the pressure difference between the injection and production wells. The data are then
251 provided to a data assimilation framework (Section 3.3) for aperture inversion, during which
252 tracer simulation is used as forward model to simulate tracer, pressure and flow rate responses
253 under various aperture scenarios. After inversion, thermal simulation is performed for both the
254 "true" and inferred aperture fields to examine the predictive ability of the inferred aperture fields.

255   The discretization of the model is as follows. The fracture plane is represented by a thin
256 layer 4 mm in thickness, and the in-plane mesh resolution is 5×5 m^2 within the circular fracture
257 and gradually increases to 150×150 m^2 in the far field. For the surrounding rock formations, the
258 mesh resolution is $5 \times 5 \times 2.5$ m^3 near the fracture plane and becomes progressively coarser in
259 the far field. The resulting computational domain consists of approximately 2,800,000 elements.
260 A massively parallel multi-physics simulation platform developed at the Lawrence Livermore
261 National Laboratory (Settgast et al., 2017), GEOS, is used for flow, tracer and thermal
262 simulation. GEOS provides a thermal-hydro-mechanical-chemical framework to simulate
263 various physical processes in subsurface reservoirs, such as fluid flow, mass and heat transport,
264 and hydraulic fracturing (Fu et al., 2013; Fu et al., 2016; Vogler et al., 2018; Wu, Fu, Morris, et
265 al., 2021). The implementation of flow, tracer and thermal modules relevant to the present study
266 has been described in the literature (Guo, Fu, Hao, & Carrigan, 2016; Guo, Fu, Hao, Peters, &
267 Carrigan, 2016), and therefore not repeated here.

268   We first simulate the flow field and then solve the advection-dispersion-sorption equation
269 based on the obtained flow field to simulate tracer transport processes. Note that we do not
270 consider mechanical simulation, indicating that the fracture aperture distribution does not evolve
271 during flow and tracer transport processes. Table 1 lists the parameters for flow and tracer
272 modeling. As the fracture plane is represented by a thin layer, we calculate the equivalent
273 porosity and permeability of the fracture through $\phi = w/H$ and $k = w^3/12H$ respectively (Guo, Fu,
274 Hao, & Carrigan, 2016), where w is the aperture and H is the thickness of the fracture layer. Due
275 to the relatively low rock formation permeability and the minor effect of matrix diffusion on
276 tracer transport (Wu, Fu, Hawkins, et al., 2021), we assume that tracer transport is confined
277 within the circular fracture and only consider the fracture for tracer modeling. Fracture
278 boundaries are assumed impermeable. A hydrostatic initial pressure is assumed in the model with
279 a pressure of 30 MPa at the fracture depth. The flow field in the fracture is simulated with an
280 injection rate of 20 L/s and a constant downhole pressure of 30 MPa at the two production wells
281 (Fig. 3(b) and (c)). According to the simulation results, the pressure difference between the
282 injection and production wells and flow rates at production well 1 and 2 are 824 kPa, 5.9 L/s, and
283 14.1 L/s respectively for the log-normal aperture field (Fig. 3(b)), and 178 kPa, 12.2 L/s, and 7.8
284 L/s respectively for the two facies aperture field (Fig. 3(c)).

285   We inject tracers into the fracture for one hour and simulate tracer transport for 20 hours
286 to obtain tracer BTCs at the two production wells (Fig. 4). We consider both conservative and
287 sorptive tracers. Note that for the simulation of a sorptive tracer, we assume an equilibrium
288 sorption process with a typical partition coefficient of 1 mm. Compared with the conservative
289 tracer BTCs, the sorptive tracer BTCs exhibit delayed peaks and reduced peak concentrations
290 due to sorption effects. The tracer BTCs from the two facies aperture field show earlier arrival

291 and larger peak concentration magnitude than that from the log-normal aperture field do,
292 especially for the BTCs at production well 1.

293   For thermal simulation, we circulate water among the injection and production wells for
294 50 years, with an injection rate of 20 L/s, an injection temperature of 50 °C, and a constant
295 downhole pressure of 30 MPa at the two production wells. The upper, lower and lateral model
296 boundaries are assumed impermeable to both fluid and heat. Parameters for thermal simulation
297 are also listed in Table 1. For the log-normal aperture field, the production temperature at
298 production well 1 decreases slower than that at production well 2 does (Fig. 4(a)), while for the
299 two facies aperture field, the production temperature at production well 1 decreases faster.

300 Table 1 Parameters for flow, tracer and thermal simulations of the EGS model.

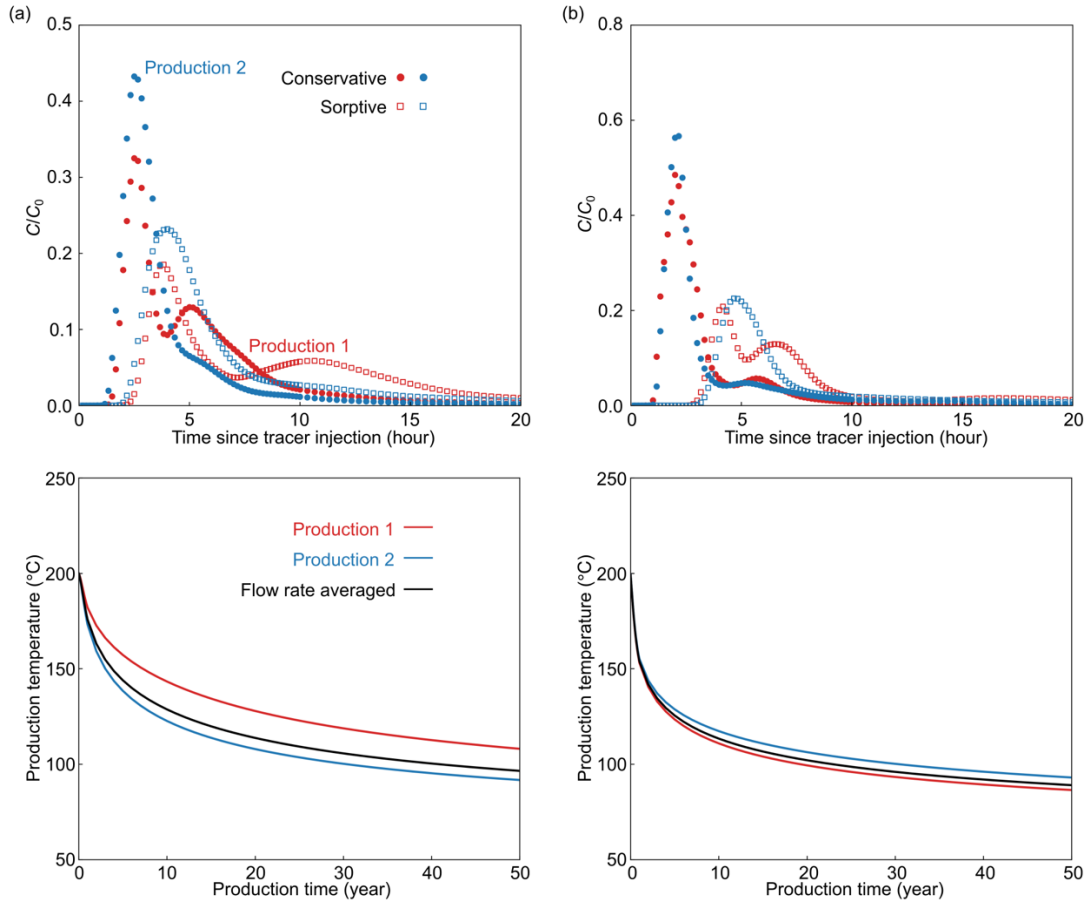| Parameter	Value
Porosity of rock matrix	0.01
Permeability of rock matrix (m^2)	1×10^{-16}
Density of rock matrix (kg/m^3)	2500
Specific heat capacity of rock matrix (J/kg/K)	790
Thermal conductivity of rock matrix (W/m/K)	2.5
Density of water (kg/m^3)	887.2
Dynamic viscosity of water (Pa·s)	1.42×10^{-4}
Compressibility of water (Pa^{-1})	5×10^{-10}
Specific heat capacity of water (J/kg/K)	4460
Longitudinal dispersivity (m)	0.2
Transverse dispersivity (m)	0.02
Partition coefficient (mm)	1

301

302

Fig. 4 Tracer (upper) and thermal (lower) breakthrough curves at the two production wells. (a) Results for the log-normal aperture field. (b) Results for the two facies aperture field. The simulated tracer concentration is normalized by injection concentration C_0.

306   3.3 A data assimilation framework for aperture inversion and thermal prediction

307   The data assimilation framework developed in Wu, Fu, Hawkins, et al. (2021) is used in
308   the current study for aperture inversion and thermal prediction. The framework includes three
309   major components, i.e., parameterization, inversion and prediction. Here we briefly introduce the
310   key procedures of applying the framework to the aperture inversion and thermal prediction in
311   this study. We refer to Wu, Fu, Hawkins, et al. (2021) for more details of the framework.

312   3.3.1 Parameterization

313   The latent spaces generated in Section 2 are used as parameter spaces for aperture
314   inversion. Five latent spaces with dimensionalities of 2, 10, 50, 200 and 800 (Fig. 1) are
315   considered. Note that the aperture field generated from the latent spaces has a square shape (800
316   m × 800 m), while the aperture field in the EGS model has a circular shape (800 m in diameter).
317   Therefore, only the field within the inscribed circle of the generated 800 m × 800 m aperture
318   field is used for flow, tracer and thermal simulation.

319   3.3.2 Aperture inversion using ES-MDA

320   The synthetic tracer, pressure and flow rate data from the "true" aperture fields (Section
321 3.2) are used for latent space inversion through ES-MDA. An advantage of ES-MDA over
322 deterministic inversion methods is that a posterior ensemble of viable realizations (instead of a
323 single optimal realization) can be obtained to quantify the uncertainties associated with the
324 aperture field. To perform ES-MDA, we first generate 720 *l*-dimensional latent parameter sets as
325 the prior ensemble by randomly sampling from the standard normal distribution. For each latent
326 parameter set in the ensemble, we use the retained principal components from PCA to map the
327 latent parameter set to an aperture field, and run flow and tracer simulation based upon the
328 aperture field. ES-MDA is then used to update the latent parameter sets according to the
329 simulated and "true" tracer, pressure and flow rate data. The two-step procedure (flow/tracer
330 simulation and latent parameter update) is repeated for 12 iterations to get the posterior
331 ensembles of latent parameter sets and aperture distributions. The major steps and update
332 equation of ES-MDA have been widely described in the literature (Emerick and Reynolds, 2013;
333 Wu, Fu, Hawkins, et al., 2021) and are not repeated here. The key parameters for ES-MDA, such
334 as data standard deviation and inflation coefficient, are the same as that in Wu, Fu, Hawkins, et
335 al. (2021). Note that 3% random Gaussian noise is added in the synthetic data before inversion
336 with ES-MDA.

337   3.3.3 Thermal prediction based on posterior aperture fields

338   After ES-MDA, the obtained posterior aperture fields are incorporated into the EGS
339 model to perform thermal simulation and predict temperature responses at the two production
340 wells. Predictions from different posterior aperture fields are used to analyze the associated
341 uncertainties.

342 **4 Aperture inversion and thermal prediction with different model complexities**

343   4.1 Comparison between "true" and simulated tracer, pressure and flow rate data

344   In each ES-MDA iteration, we record the simulation results (tracer, pressure and flow
345 rate) to compare with the "true" data (Figs. 5 and 6). The latent space dimensionality (*l*) shows
346 similar effects on the fit of tracer/pressure/flow rate data for the log-normal and two facies
347 aperture fields, as summarized below.

348   •   For *l* = 2, the simulated tracer BTCs, pressure and flow rates show little variation
349   among the 720 prior realizations (before ES-MDA) (Figs. 5(a) and 6(a)). This is because
350   the aperture fields generated from such a low-dimensional latent space have little
351   variance and are relatively smooth (i.e., low model complexity), as shown in the first
352   column of Figs. 7 and 8. After ES-MDA, the 720 parameter sets collapse to the same
353   posterior parameter set (Fig. S1 in the Supporting Information), similar to the small
354   ensemble size-induced ensemble collapse phenomenon reported in many previous studies
355   (Nejadi et al., 2017; Xiao & Tian, 2020). However, the simulation results from this
356   posterior parameter set cannot correctly fit the "true" data (Figs. 5(a) and 6(a)), which is
357   an indicator of underfitting. The second peak of the tracer BTC at production well 1 is
358   not resolved as the underlying aperture model is unable to capture the complexities in the
359   "true" aperture fields.

360   •   When l increases to ten, the complexity of the aperture model increases and the
361   variation among the prior simulation results also increases (Figs. 5(b) and 6(b)).
362   Nevertheless, the 720 parameter sets still collapse to the same posterior parameter set
363   after ES-MDA (Fig. S1). The fit of the "true" data, especially the pressure and flow rate
364   data, is better than that for $l = 2$. The second peak of the tracer BTC at production well 1
365   is successfully resolved by the posterior realizations, although there still exist some
366   discrepancies between the "true" and simulated tracer BTCs.
367   •   When l further increases to 50, the collapse of parameter sets is greatly alleviated
368   and the posterior latent parameters show considerable uncertainties (Fig. S1).
369   Correspondingly, the uncertainty of the simulation results from the posterior ensemble
370   also increases, especially for the tracer BTCs (Figs. 5(c) and 6(c)). The 90% credible
371   intervals of the simulated tracer BTCs properly match the "true" tracer BTCs, and both
372   the arrival time and magnitude of the second peak of the tracer BTC at production well 1
373   are correctly reproduced. An aperture model with moderate complexity is able to capture
374   the necessary variations in the "true" aperture field to reproduce the tracer, pressure and
375   flow rate data, even if the aperture model and the true" aperture field follow
376   fundamentally different statistical distributions.
377   •   When l increases to 200 and 800, the latent parameter uncertainties in the
378   obtained posterior ensemble further increase (Fig. S1), and the simulation results from the
379   posterior ensemble show even larger uncertainties compared with that for $l = 50$ (Figs.
380   5(d), 5(e), 6(d) and 6(e)). With a relatively large latent space dimensionality, the tracer
381   BTCs, pressure and flow rate data can be matched but the associated uncertainties are
382   significant. Further analysis of the predictive ability of the obtained posterior realizations
383   is necessary to examine possible overfitting of the inversion results.
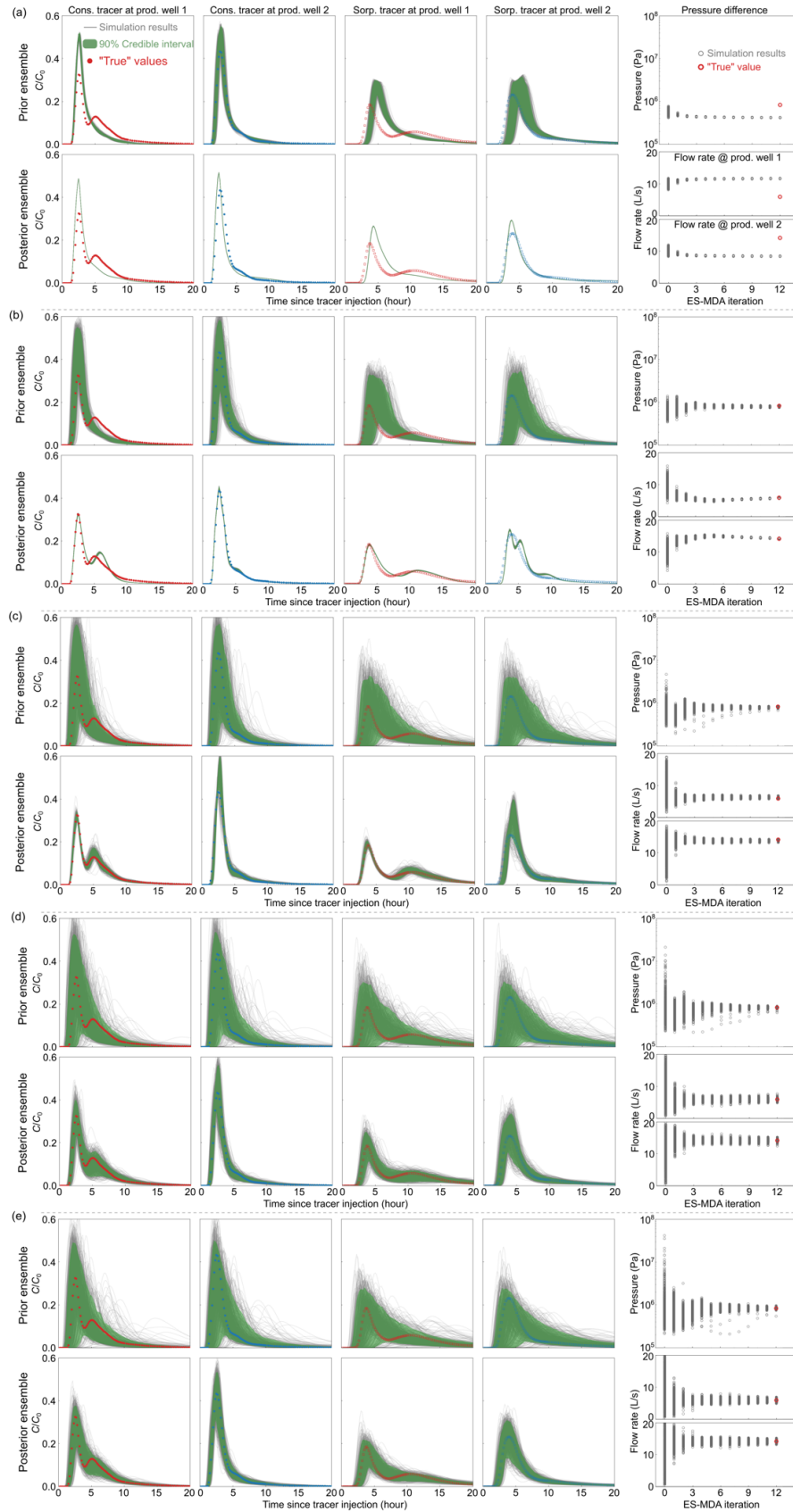
384

385   Fig. 5 Comparison of tracer BTCs, pressure and flow rates between the "true" data and the
386   simulation results for the log-normal aperture scenario. (a) Inversion with a latent space
387   dimensionality of $l = 2$. (b) $l = 10$. (c) $l = 50$. (d) $l = 200$. (e) $l = 800$. For tracer BTCs (the first to
388   fourth columns), the upper row shows the results from prior realizations, and the lower row
389   shows the results from posterior realizations. Note that we show the tracer BTCs from all the 720
390   realizations (grey curves), as well as the corresponding 90% credible intervals (green shadings).
391   For pressure difference and flow rate (the fifth column), we show the evolution of simulation
392   results (grey circles) with respect to ES-MDA iterations. The "true" values are annotated by red
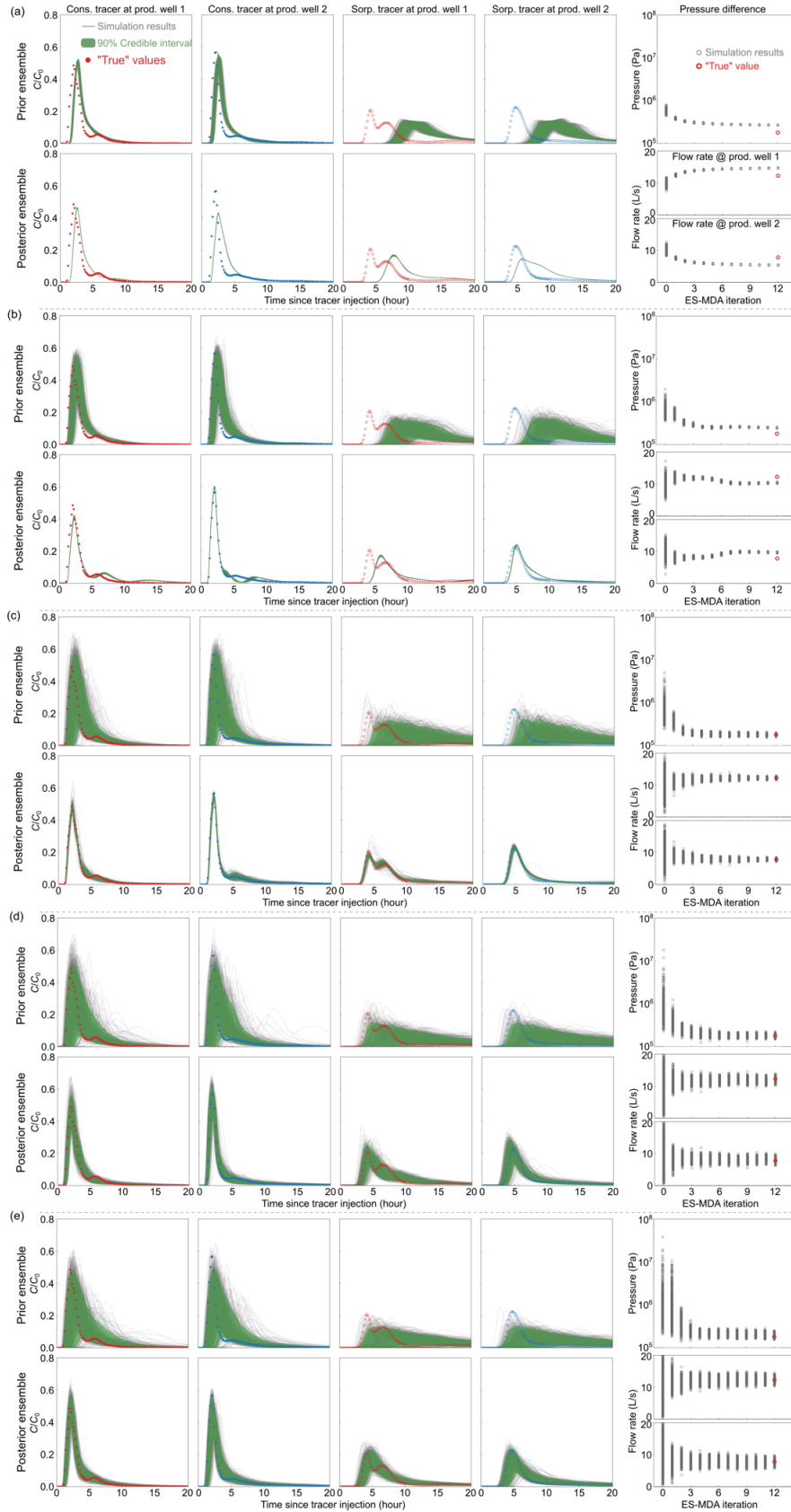393   circles situated along the final iteration.

394

395   Fig. 6 Comparison of tracer BTCs, pressure and flow rates between the "true" data and the
396   simulation results for the two facies aperture scenario. (a) Inversion with a latent space
397   dimensionality of $l = 2$. (b) $l = 10$. (c) $l = 50$. (d) $l = 200$. (e) $l = 800$.

398   4.2 Aperture distribution and flow field in the fracture

399   We now analyze the aperture distribution and flow field in the fracture (Figs. 7 and 8).
400   We generate aperture distributions from the prior and posterior ensembles, and then perform
401   flow simulations to obtain the corresponding flow fields. For both the log-normal and two facies
402   aperture scenarios, we observe some narrow flow channels connecting the injection and
403   production wells in the "true" flow fields (Fig. 3). When the latent space dimensionality is low (l
404    $= 2$), the aperture field generated from PCA is relatively smooth, and the posterior aperture
405   distributions cannot resolve these narrow flow channels (first column of Figs. 7 and 8). A larger
406   latent space dimensionality leads to a more heterogeneous aperture distribution and therefore a
407   more channelized flow field. When the latent space dimensionality is high, both the prior and
408   posterior realizations exhibit some narrow channels between the injection and production wells
409   (Figs. 7 and 8). Of course, as the prior realization is not conditioned on the tracer, pressure and
410   flow rate data, the corresponding flow field is significantly different from the "true" flow field.
411   For example, the flow field from a prior realization with $l = 800$ (second row, fifth column in
412   Fig. 7) shows two major channels connecting the injection well and production well 2, but
413   misses the channel between the injection well and production well 1. After ES-MDA, the
414   obtained posterior realization shows a flow field that resembles the "true" flow field better than
415   the prior realization does, especially for the high latent space dimensionality cases (fourth row in
416   Figs. 7 and 8).

417   However, not every flow channel in the "true" flow field is resolved by the posterior
418   realizations. For the log-normal aperture scenario, the "true" flow field shows four major and
419   several minor flow channels between the injection and production wells (Fig. 3(b)), while the
420   posterior realizations only resolve three major flow channels (sixth row in Fig. 7). For the two
421   facies aperture scenario, there are seven flow channels in the "true" flow field (Fig. 3(c)), but
422   only two major flow channels in the flow fields from the posterior realizations (sixth row in Fig.
423   8). Compared with the "true" flow fields, the flow fields from posterior realizations have fewer
424   flow channels but larger channel width. The relatively large channel width is necessary for the
425   posterior realizations to maintain comparable effective fracture areas as that in the "true" flow
426   fields, so that the tracer, pressure and flow rate data can be matched (especially the sorptive
427   tracer BTC which highly depends on the interaction area between fracture fluid and surrounding
428   rocks). The overall effect of the many narrow flow channels in the "true" flow field is
429   represented by the two or three relatively wide flow channels in the flow fields from posterior
430   realizations.

431   The latent space dimensionality shows significant effect on the posterior aperture
432   distributions. For a small latent space dimensionality ($l = 2$ or 10), the posterior aperture
433   distributions (flow fields) are almost identical, which is a direct consequence of latent parameter
434   collapse. Besides the randomly selected posterior realization in Figs. 7 and 8 (third and fourth
435   rows in Fig. 7 for the log-normal aperture scenario, and in Fig. 8 for the two facies aperture
436   scenario), we provide two additional, randomly selected posterior realizations for comparison in
437   the Supporting Information (Fig. S2). All the three aperture distributions (flow fields) are almost
438   the same as the average aperture distribution (flow field) displayed in the fifth and sixth rows in

439 Figs. 7 and 8. The standard deviation of the posterior realizations is negligible (Fig. S3 in the
440 Supporting Information). With the increase of latent space dimensionality, the variations among
441 the posterior aperture distributions (flow fields) increase (Fig. S3). The uncertainty in the latent
442 parameters propagates to the aperture distribution and flow field. For a large latent space
443 dimensionality ($l = 200$ or 800), we observe considerable variations in aperture distribution
444 among the posterior realizations, but the major flow channels from these posterior realizations
445 are similar, as a result of conditioning on tracer, pressure and flow rate data.

446   In the next section, we will analyze how the uncertainty in the latent parameters further
447 propagates to thermal predictions and examine possible overfitting of the posterior realizations
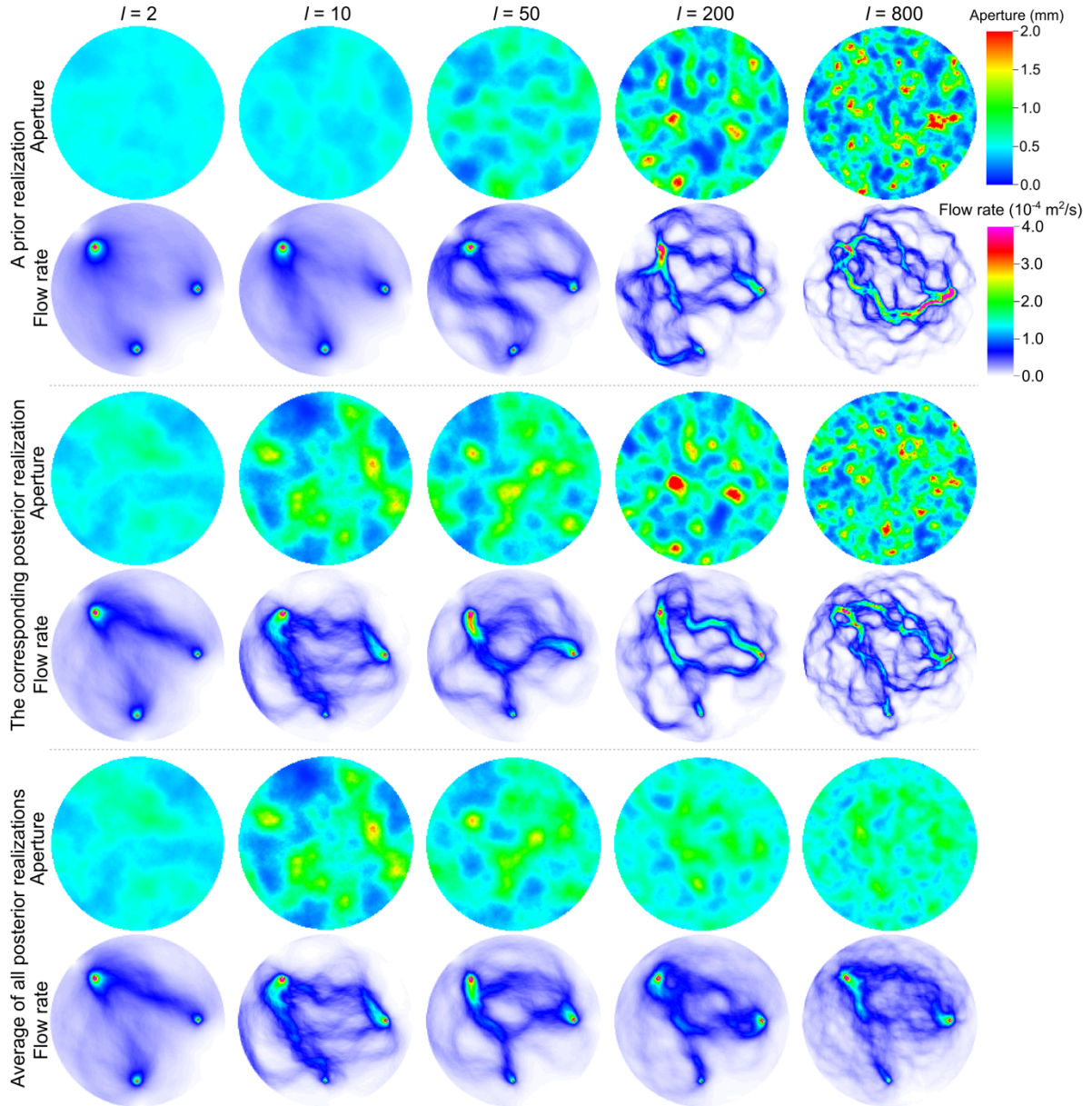448 obtained with a relatively large latent space dimensionality.

449

Fig. 7 Aperture distribution and flow field in the fracture for the log-normal aperture scenario. The first and second rows are results from a randomly selected realization in the prior ensemble (before ES-MDA), and the third and fourth rows are results from the corresponding posterior realization (after 12 ES-MDA iterations). The fifth and sixth rows are average results of all the realizations in the posterior ensemble.
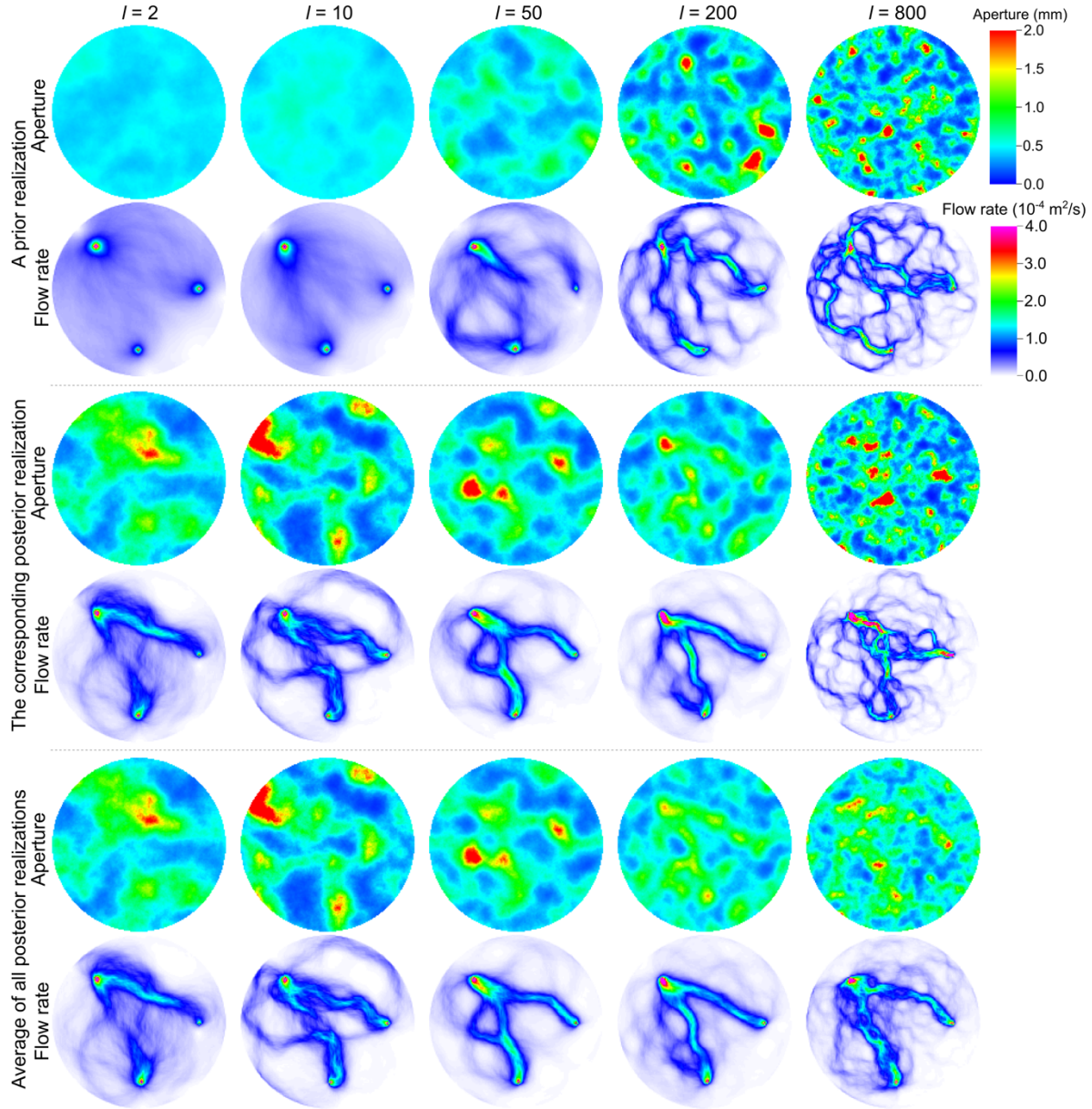

Fig. 8 Aperture distribution and flow field in the fracture for the two facies aperture scenario. The first and second rows are results from a randomly selected realization in the prior ensemble (before ES-MDA), and the third and fourth rows are results from the corresponding realization in the posterior ensemble (after 12 ES-MDA iterations). The fifth and sixth rows are average results of all the realizations in the posterior ensemble.

461   4.3 Thermal performance prediction

462   In this sub-section, we perform thermal simulations with both prior and posterior
463   realizations to analyze their abilities in predicting the long-term thermal performance of the EGS
464   model. For each latent space dimensionality, we randomly select ten prior realizations and their
465   corresponding posterior realizations to perform thermal simulation, and then compare the
466   simulated temperature responses with the "true" temperature responses (Figs. 9 and 10).

467   We first analyze the prior predictions (first and third rows in Figs. 9 and 10). With the
468   increase of latent space dimensionality, the variations among the prior predictions of temperature
469   responses increase (first row in Figs. 9 and 10). For relatively large latent space dimensionalities,
470   the prior predictions vary in broad ranges and many predictions significantly underestimate the
471   temperature reductions. Interestingly, the variation among the prior predictions of the flow rate-
472   averaged temperature response (third row in Figs. 9 and 10), although considerable for large
473   latent space dimensionality cases, is substantially smaller than that of the temperature responses
474   at individual production wells. To understand the reduced variation of the flow rate-averaged
475   temperature response, we select a prior realization for further analysis (Fig. 11). For the prior
476   realization, the predicted flow rate at production well 1 is 2.7 L/s, much smaller than the "true"
477   flow rate (5.9 L/s). As a result, the predicted flow rate at production well 2 is much larger than
478   the corresponding "true" flow rate. The temperature decrease is highly related to the flow rate.
479   The underestimated flow rate at production well 1 results in a slow temperature decrease at
480   production well 1, and the overestimated flow at production well 2 leads to a fast temperature
481   decrease at production well 2. Since the flow rates at the two production wells are not
482   independent, the underestimation of flow rate at one production well means the overestimation of
483   flow rate at the other production well. Therefore, when the temperature decrease at one
484   production well is significantly underestimated (e.g.: production well 1 in Fig. 11(a)), the
485   temperature decrease at the other production well is likely to be overestimated (production well 2
486   in Fig. 11(a)). As a result, the variation of the temperature prediction at one production well
487   counteracts the variation of the temperature prediction at the other production well, causing a
488   reduced variation in the flow-rated averaged temperature prediction.

489   Compared with prior realizations, the posterior realizations provide more accurate
490   predictions for both the individual and flow-rate averaged temperature responses (second and
491   fourth rows in Figs. 9 and 10). When latent space dimensionality is low ($l = 2$ or 10), temperature
492   predictions from the ten posterior realizations are almost identical due to the collapse of latent
493   parameters, and cannot match the "true" temperature responses. With the increase of latent space
494   dimensionality, the posterior predictions match the "true" temperature responses better but also
495   show larger uncertainties. When the latent space dimensionality increases to 800, the posterior
496   predictions at individual production wells exhibit significant uncertainties, indicating the
497   overfitting of the obtained posterior realizations. However, the posterior prediction of the flow-
498   rated averaged temperature response still successfully reproduces the "true" response with
499   relatively small uncertainty (fourth row, fifth column in Figs. 9 and 10). Once again this is
500   mainly caused by the counteraction between the underestimation of temperature response at one
501   production well and the overestimation of temperature response at the other production well, as
502   shown by the example in Fig. 11(b).

503   According to Figs. 9 and 10, to correctly predict the thermal responses at the two
504   production wells, the latent space dimensionality should be in the range of 10 ~ 200 for the log-
505   normal aperture scenario, and 50 ~ 200 for the two facies aperture scenario. While for the flow-

19

506 rated averaged temperature response, the latent space dimensionality should not be smaller than
507 ten for the log-normal aperture scenario, and a larger latent space dimensionality not smaller than
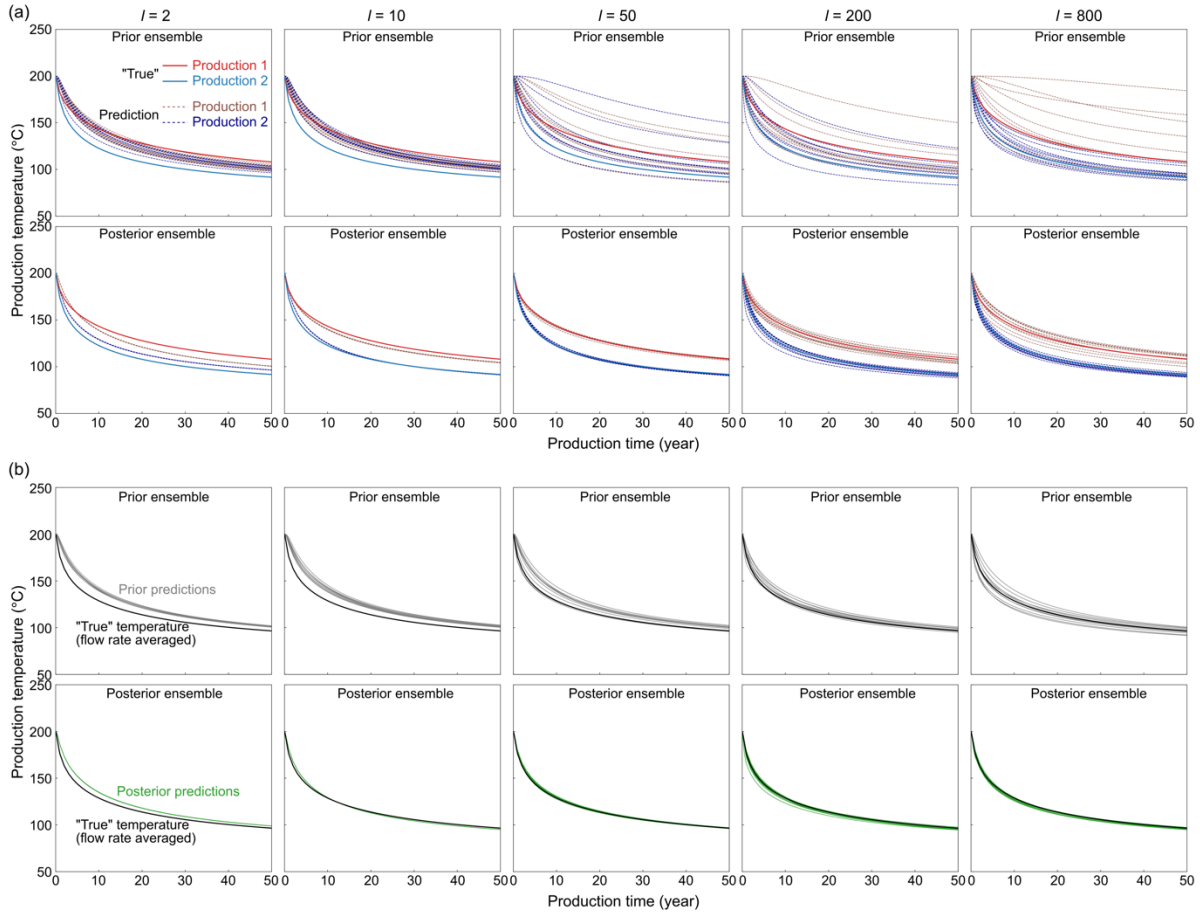508 50 appears to be necessary for the two-facies aperture scenario.

509

510 Fig. 9 Prediction of thermal responses from prior and posterior realizations for the log-normal
511 aperture scenario. (a) Temperature responses at the two production wells. The solid lines are
512 "true" temperature responses, and the dash lines are predictions. The upper row shows the
513 predictions from prior realizations, and the lower row shows the predictions from posterior
514 realizations. (b) Flow rate averaged temperature response. The black line is the "true"
515 temperature response. The gray and green lines are predictions from prior (upper row) and
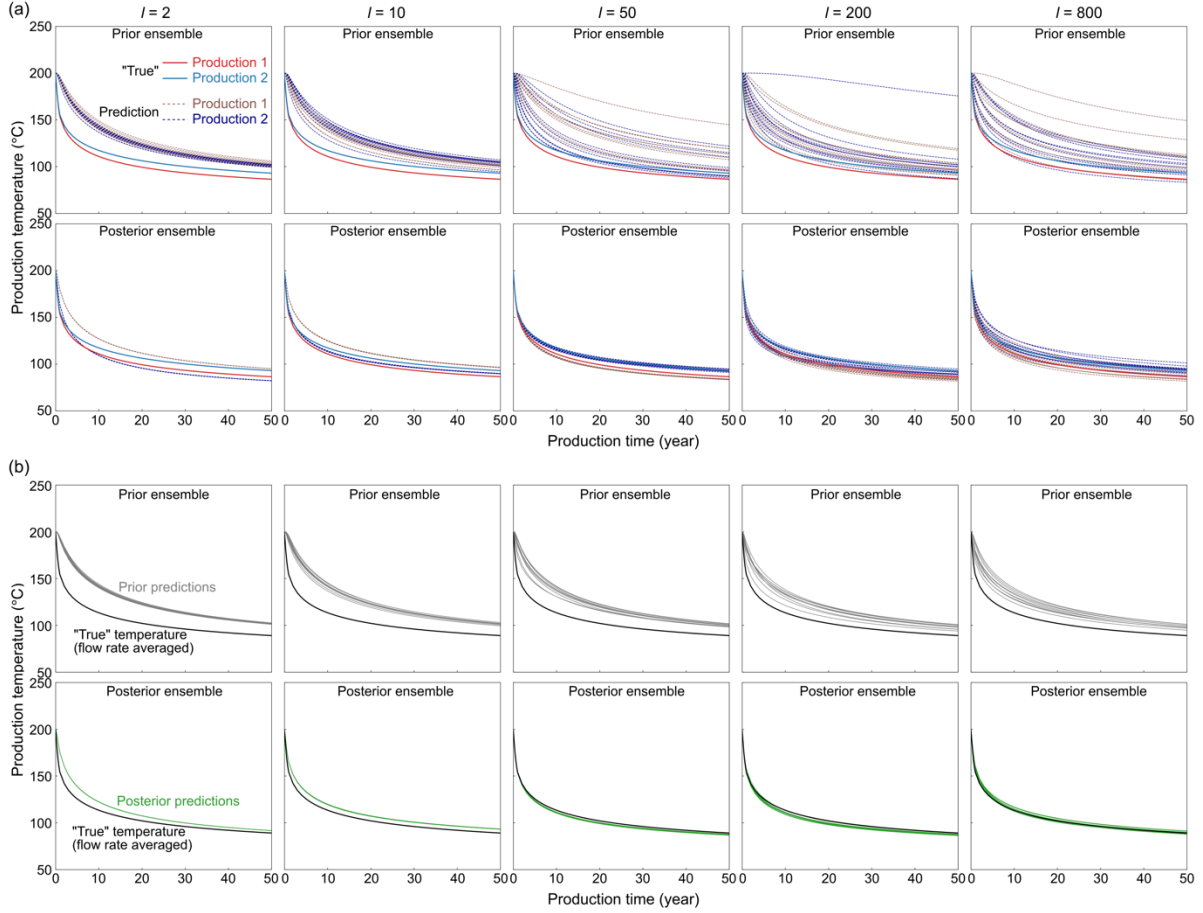516 posterior (low row) realizations respectively.

517

518 Fig. 10 Prediction of thermal responses from prior and posterior realizations for the two facies
519 aperture scenario. (a) Temperature responses at the two production wells. (b) Flow rate averaged
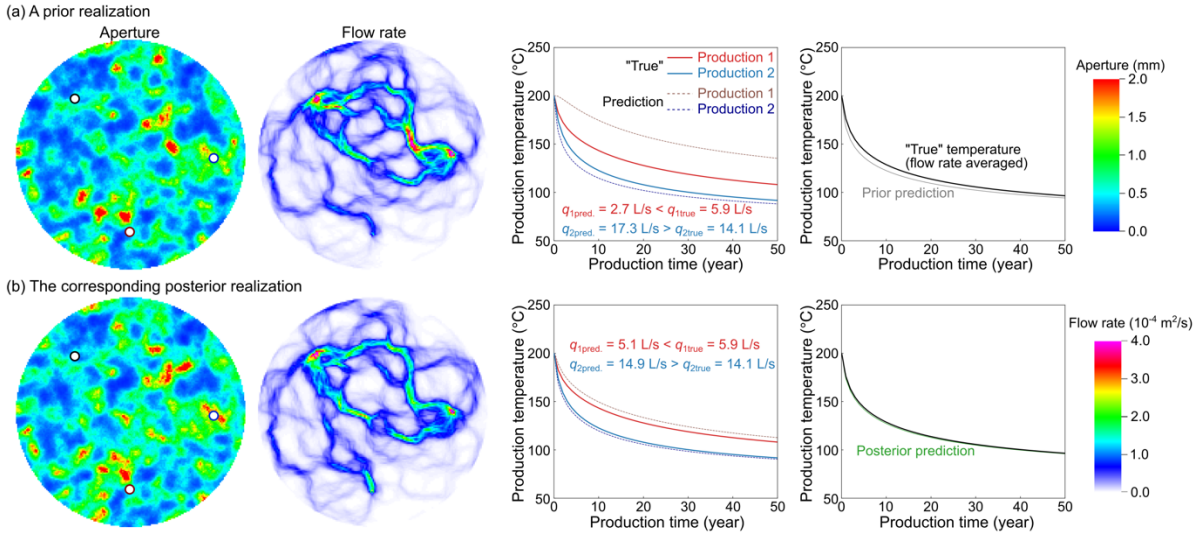520 temperature response.

521

522 Fig. 11 Comparison of aperture distribution, flow field and temperature responses between a prior
523 realization and the corresponding posterior realization. The prior and posterior realizations are
524 from the ES-MDA case with a latent dimensionality of 800 for the log-normal aperture scenario.

525   Predicted ($q_{1pred.}$ and $q_{2pred.}$) and true (q_{1true} and q_{2true}) flow rates at the two production wells are
526   annotated.

5 Discussion

528   5.1 Selecting appropriate model complexity

529   Model reduction has been considered essential to tackle the challenges associated with
530   complex subsurface conditions and data scarcity in many subsurface inversion and
531   characterization problems (Jiang & Ou, 2017; Marzouk & Najm, 2009; Zhu & Zabaras, 2018).
532   The present study attempts to investigate the effect of model complexity on the inversion and
533   prediction of subsurface reservoirs, and more importantly, to provide some insights into the
534   selection of model complexity to avoid underfitting and overfitting. Through a field-scale EGS
535   model, we demonstrate both underfitting behavior under low model complexity (poor data
536   match) and overfitting behavior under high model complexity (good data match but poor
537   prediction). For the log-normal aperture scenario considered in the present study, an inversion
538   model that preserves 21% of the total variance in the "true" aperture field (corresponding to a
539   latent space dimensionality of $l = 50$) is sufficient to correctly reproduce tracer/pressure/flow rate
540   data and accurately predict long-term thermal performance. Increasing the model complexity to
541   preserve 56% of the total variance ($l = 200$) can also produce satisfactory data fit and thermal
542   prediction results but the associated uncertainties increase. Further increasing the model
543   complexity to preserve 84% of the total variance ($l = 800$) leads to significant uncertainties and
544   the thermal performance cannot be accurately predicted. Therefore, a model corresponds to a
545   latent space dimensionality between 50 and 200, i.e., with 21% to 56% of the total variance
546   preserved, is appropriate for tracer/pressure/flow rate data inversion and thermal prediction in the
547   present study. This is also true for the two facies aperture scenario where the "true" aperture field
548   and the aperture model used for inversion follow different statistical distributions.

549   The selection of model complexity actually depends on the purpose of inversion. For the
550   presented EGS model, we note that although the posterior aperture fields obtained from the latent
551   space with $l = 50$ (Figs. 7, 8 and S2) can reproduce the "true" data and make accurate
552   predictions, they look different from the "true" aperture fields in Fig. 3. Many fine features in the
553   "true" aperture field could not be resolved due to the lack of necessary complexities in the
554   aperture model generated from such a low-dimensional latent space. Hence, if the primary goal is
555   to infer fracture aperture, a relatively high model complexity is required, but if the primary goal
556   is to predict thermal performance, then a moderate model complexity is sufficient. For many
557   subsurface characterization problems, people are mainly concerned with the predictive ability
558   rather than the realism of the inversion results, and therefore a moderate model complexity could
559   be employed.

560   The selection of model complexity also needs to consider the amount of information
561   contained in the data for inversion. In general, the more information the data contain, the more
562   complex the model should be to avoid underfitting. In the present study, the inversion data
563   include tracer BTCs/flow rates at two production wells and pressure difference between injection
564   and production wells. The information in these data is spatially limited and far from sufficient to
565   characterize the aperture distribution in the 2D fracture plane. As a result, a relatively simple
566   model is able to retrieve the information and reproduce the data. Fortunately, since both tracer
567   transport and heat extraction processes are tightly related to the flow field among the injection

568   and production wells, the information retrieved from tracer BTCs, although limited, still provide
569   accurate thermal predictions. If more data, for example, tracer BTCs at other locations are
570   available, the model complexity needs to be increased to accommodate the increased amount of
571   information in the inversion data.

572   The result that a model preserving only 21% of the total variance in the "true" aperture
573   field is able to reproduce tracer/pressure/flow rate data and predict thermal responses is
574   surprising as many studies preserved at least 50% ~ 60% total variance when using PCA for
575   model reduction (Fernández-Martínez et al., 2012; Hawkins et al., 2020; Laloy et al., 2013). An
576   important implication from the current study is that we should use a relatively simple model for
577   inversion/data assimilation in subsurface reservoirs, especially when the available measurements
578   are scarce and prediction is the primary goal. A low complexity model can not only mitigate the
579   overfitting pitfall but also alleviate the computational burden in many subsurface inversion
580   problems. Of course, the model should not be too simple otherwise it may fail to reproduce
581   inversion data.

582   5.2 Geologic facies model

583   Geologic facies models have been used to describe highly channelized subsurface
584   reservoirs such as the two facies aperture model in Fig. 3(c). The characterization of such facies
585   models has been widely investigated in recent years (Chang et al., 2010; Jafarpour
586   & McLaughlin, 2009; Jiang & Jafarpour, 2021). To preserve the geologic realism of facies
587   models during inversion/data assimilation, a model reduction method that can directly generate
588   facies models from low-dimensional latent space is required. PCA is inappropriate as facies
589   models do not follow a Gaussian or log-normal distribution. Many methods have been proposed
590   for the reduction of facies models, such as optimization-based PCA (Vo & Durlofsky, 2014),
591   discrete cosine transform (Jafarpour & McLaughlin, 2007), and deep learning algorithms such as
592   variational autoencoder (VAE) (Canchumuni et al., 2019; Laloy et al., 2017; Mo et al., 2020) and
593   generative adversarial network (GAN) (Canchumuni et al., 2020; Laloy et al., 2018).

594   The current study provides an alternative strategy for the characterization of geologic
595   facies models. Instead of developing advanced model reduction methods for the two facies
596   aperture model in Fig. 3(c), we directly use a log-normal aperture model generated from PCA
597   latent space for data assimilation. Although the "true" and inversion aperture models follow
598   fundamentally different statistical distributions, the obtained posterior aperture models are able
599   to reproduce tracer/pressure/flow rate data and predict long-term thermal performance after data
600   assimilation. A log-normal aperture model with appropriate correlation length is capable of
601   inducing relevant channelized flow structures analogous to those of a facies-based model. The
602   posterior aperture distributions fail to preserve the geologic realism in the two facies aperture
603   model (Fig. 8). However, as Murray (2007) concluded, if prediction instead of explanation is the
604   primary goal, the realism of model parameters should not be considered an essential model-
605   evaluation criterion.

606   5.3 Prior realization

607   An interesting observation is that a prior aperture realization and the corresponding
608   posterior aperture realization have many common features, especially when the aperture model is
609   relatively complex (fourth and fifth columns in Figs. 7 and 8, Fig. 11). In another words, ES-
610   MDA tends to perturb a prior realization as slightly as possible to match the data being

611 assimilated. The obtained posterior realization largely depends on the prior realization provided
612 to ES-MDA. If the prior realization is not well constrained or even physically unrealistic, then
613 the corresponding posterior realization may also show unrealistic features. Therefore, it is of
614 great importance to constrain prior realizations with available prior knowledge. Fortunately, for
615 subsurface reservoirs, prior knowledge of the field of interest (aperture or permeability) can be
616 obtained from geological/geophysical measurements, such as core logs, wellbore images and
617 outcrop analysis. In the current study, the prior knowledge used to constrain prior aperture
618 realizations includes the spatially autocorrelated nature as well as the mean, standard deviation
619 and correlation length of the aperture field.

620 Interpretation results from other geophysical investigations, such as seismic and ground
621 penetrating radar (GPR), can also be used to constrain prior realizations. For example, Wu, Fu,
622 Hawkins, et al. (2021) used the results of GPR survey to constrain prior aperture realizations in a
623 horizontal fracture at a meso-scale field test site (the Altona Field Laboratory located in northern
624 New York State, USA). The GPR survey of the field test site indicated a narrow flow channel
625 between injection and production wells, which meant that the underlying aperture field was
626 anisotropic with larger correlation length in the direction from injection to production wells
627 (west to east) than that in the south to north direction. During subsequent tracer data assimilation,
628 such an anisotropic feature was used as prior knowledge to constrain prior aperture realizations.

6 Conclusion

630 We investigated the effect of model complexity on the inversion of fracture aperture
631 distribution as well as the prediction of long-term thermal recovery in a field-scale EGS model.
632 Inversion models with different complexities were used to invert for fracture aperture
633 distribution through the assimilation of tracer/pressure/flow rate data using an ensemble-based
634 method (ES-MDA). Thermal simulations were then performed to examine the predictive ability
635 of the inferred aperture distributions. With a low model complexity, ensemble collapse occurred.
636 The inferred aperture distributions failed to reproduce tracer/pressure/flow rate data, and the
637 predicted long-term thermal response was biased. With a high complexity model, the data could
638 be properly matched, but the inferred aperture distribution and predicted thermal response
639 exhibit significant uncertainties. A moderate model complexity is sufficient to retrieve the
640 information contained in tracer/pressure/flow rate data and provide accurate thermal predictions.

641 An appropriate model complexity is essential to the inversion and prediction of
642 subsurface reservoirs, and deserves careful deliberation based on the primary purpose of the
643 inversion as well as the type and amount of the inversion data. In a real-world application, it is
644 difficult to predetermine model complexity and one might need to manually adjust model
645 complexity in a trial-and-error manner. According to the results in the current study, we
646 recommend starting with a relatively simple model rather than an extremely complex model, and
647 the quality of the fit to tracer BTCs appears to be a reasonable indicator of an appropriate model
648 complexity.

649

Data Availability Statement

651 The synthetic flow, pressure, tracer and thermal data used in this study is obtained from
652 numerical simulations with GEOS. The data assimilation framework is available in Wu, Fu,
653 Hawkins, et al. (2021).

654

References

Berkowitz, B. (2002). Characterizing flow and transport in fractured geological media: A review. *Advances in Water Resources*, *25*, 861-884. https://doi.org/10.1016/S0309-1708(02)00042-8

Canchumuni, S. W. A., Castro, J. D. B., Potratz, J., Emerick, A. A., & Pacheco, M. A. C. (2020). Recent developments combining ensemble smoother and deep generative networks for facies history matching. *Computational Geosciences*, *25*, 433-466. https://doi.org/10.1007/s10596-020-10015-0

Canchumuni, S. W. A., Emerick, A. A., & Pacheco, M. A. C. (2019). Towards a robust parameterization for conditioning facies models using deep variational autoencoders and ensemble smoother. *Computers & Geosciences*, 128, 87-102. https://doi.org/10.1016/j.cageo.2019.04.006

Chang, H., Zhang, D., & Lu, Z. (2010). History matching of facies distribution with the EnKF and level set parameterization. *Journal of Computational Physics*, 229, 8011-8030. https://doi.org/10.1016/j.jcp.2010.07.005

Chen, X., Hammond, G. E., Murray, C. J., Rockhold, M. L., Vermeul, V. R., & Zachara, J. M. (2013). Application of ensemble-based data assimilation techniques for aquifer characterization using tracer data at Hanford 300 area. *Water Resources Research*, *49*(10), 7064-7076. https:// doi.org/10.1002/2012WR013285

Chen, Y., & Zhao, Z. (2020). Heat transfer in a 3D rough rock fracture with heterogeneous apertures. *International Journal of Rock Mechanics and Mining Sciences*, 134, 104445. https://doi.org/10.1016/j.ijrmms.2020.104445

Cox, S. F., Knackstedt, M. A., & Braun, J. (2001). Principles of structural control on permeability and fluid flow in hydrothermal systems. *Reviews in Economic Geology*, 14, 1-24. https://doi.org/10.5382/Rev.14.01

Dobson, P. F., Kneafsey, T. J., Hulen, J., & Simmons, A. (2003). Porosity, permeability, and fluid flow in the Yellowstone geothermal system, Wyoming. *Journal of Volcanology and Geothermal Research*, 123, 313-324. https://doi.org/10.1016/S0377-0273(03)00039-8

Emerick, A. A. (2017). Investigation on principal component analysis parameterizations for history matching channelized facies models with ensemble-based data assimilation. *Mathematical Geosciences*, 49(1), 85-120. https://doi.org/10.1007/s11004-016-9659-5

Emerick, A. A. (2018). Deterministic ensemble smoother with multiple data assimilation as an alternative for history-matching seismic data. *Computational Geosciences*, *22*(5), 1175-1186. https://doi.org/10.1007/s10596-018-9745-5

Emerick, A. A., & Reynolds, A. C. (2013). Ensemble smoother with multiple data assimilation. *Computers & Geosciences*, 55, 3-15. https://doi.org/10.1016/j.cageo.2012.03.011

Fernández-Martínez, J. L., Mukerji, T., García-Gonzalo, E., & Suman, A. (2012). Reservoir characterization and inversion uncertainty via a family of particle swarm optimizers. Geophysics, 77(1), M1-M16. https://doi.org/10.1190/geo2011-0041.1

Fu, P., Hao, Y., Walsh, S. D. C., & Carrigan, C. R. (2016). Thermal drawdown-induced flow channeling in fractured geothermal reservoirs. *Rock Mechanics and Rock Engineering*, 49(3), 1001–1024. https://doi.org/10.1007/s00603-015-0776-0

Fu, P., Johnson, S. M., & Carrigan, C. R. (2013). An explicitly coupled hydro-geomechanical model for simulating hydraulic fracturing in arbitrary discrete fracture networks. *International Journal for Numerical and Analytical Methods in Geomechanics*, 37, 2278-2300. https://doi.org/10.1002/nag.2135

Guo, B., Fu, P., Hao, Y., & Carrigan, C. R. (2016). Investigating the possibility of using tracer tests for early identification of EGS reservoirs prone to flow channeling. 41st workshop on geothermal reservoir engineering.

Guo, B., Fu, P., Hao, Y., Peters, C. A., & Carrigan, C. R. (2016). Thermal drawdown-induced flow channeling in a single fracture in EGS. *Geothermics*, 61, 46-62. https://doi.org/10.1016/j.geothermics.2016.01.004

Hawkins, A. J., Fox, D. B., Koch, D. L., Becker, M. W., & Tester, J. W. (2020). Predictive inverse model for advective heat transfer in a short-circuited fracture: Dimensional analysis, machine learning, and field demonstration. *Water Resources Research*, 56, e2020WR027065. https:// doi.org/10.1029/2020WR027065

Jafarpour, B., & McLaughlin, D. B. (2007). Efficient permeability parameterization with the discrete cosine transform. *SPE reservoir simulation symposium*.

Jafarpour, B., & McLaughlin, D. B. (2009), Estimating channelized-reservoir permeabilities with the ensemble Kalman filter: The importance of ensemble design. *SPE Journal*, 14(2), 374-388. https://doi.org/10.2118/108941-PA

Jiang, A., & Jafarpour, B. (2021). Deep convolutional autoencoders for robust flow model calibration under uncertainty in geologic continuity. *Water Resources Research*, 57(11), e2021WR029754. https://doi.org/10.1029/2021WR029754

Jiang, L., & Ou, N. (2017). Multiscale model reduction method for Bayesian inverse problems of subsurface flow. *Journal of Computational and Applied Mathematics*, 319, 188-209. https://doi.org/10.1016/j.cam.2017.01.007

Jiang, Z., Zhang, S., Turnadge, C., & Xu, T. (2021). Combining autoencoder neural network and Bayesian inversion to estimate heterogeneous permeability distributions in enhanced geothermal reservoir: Model development and verification. *Geothermics*, 97, 102262. https://doi.org/10.1016/j.geothermics.2021.102262

Johnson, T. C., Burghardt, J., Strickland, C., Knox, H., Vermeul, V., White, M., et al. (2021). 4D proxy imaging of fracture dilation and stress shadowing using electrical resistivity tomography during high pressure injections into a dense rock formation. *Journal of Geophysical Research: Solid Earth*, 126, e2021JB022298. https://doi.org/10.1029/2021JB022298

742 Laloy, E., Hérault, R., Jacques, D., & Linde, N. (2018). Training-image based geostatistical
743   inversion using a spatial generative adversarial neural network. *Water Resources*
744   *Research*, 54, 381-406. https://doi.org/10.1002/ 2017WR022148
745 Laloy, E., Hérault, R., Lee, J., Jacques, D., & Linde, N. (2017). Inversion using a new low-
746   dimensional representation of complex binary geo- logical media based on a deep neural
747   network. *Advances in Water Resources*, 110, 387-405.
748   https://doi.org/10.1016/j.advwatres.2017.09.029
749 Laloy, E., Rogiers, B., Vrugt, J. A., Mallants, D., & Jacques, D. (2013). Efficient posterior
750   exploration of a high-dimensional groundwater model from two-stage Markov chain
751   Monte Carlo simulation and polynomial chaos expansion. *Water Resources Research*,
752   49(5), 2664-2682. https://doi.org/10.1002/wrcr.20226
753 Li, W., & Cirpka, O. A. (2006). Efficient geostatistical inverse methods for structured and
754   unstructured grids. *Water Resources Research*, 42, W06402.
755   https://doi.org/10.1029/2005WR004668
756 Liu, M., & Grana, D. (2020). Petrophysical characterization of deep saline aquifers for CO_2
757   storage using ensemble smoother and deep convolutional autoencoder. *Advances in*
758   *Water Resources*, *142*, 103634. https://doi.org/10.1016/j.advwatres.2020.103634
759 Liu, Y., & Durlofsky, L. J. (2020). 3D CNN-PCA: A deep-learning-based parameterization for
760   complex geomodels. *Computers & Geosciences*, 148, 104676.
761   https://doi.org/10.1016/j.cageo.2020.104676
762 Marzouk, Y. M., & Najm, H. N. (2009). Dimensionality reduction and polynomial chaos
763   acceleration of Bayesian inference in inverse problems. *Journal of Computational*
764   *Physics*, 228(6), 1862-1902. https://doi.org/10.1016/j.jcp.2008.11.024
765 Mo, S., Zabaras, N. J., Shi, X., & Wu, J. (2020). Integration of adversarial autoencoders with
766   residual dense convolutional networks for estimation of non-Gaussian hydraulic
767   conductivities. *Water Resources Research*, 56, e2019WR026082. https://doi.org/10.
768   1029/2019WR026082
769 Murray, A. B. (2007). Reducing model complexity for explanation and prediction.
770   *Geomorphology*, 90, 178-191. https://doi.org/10.1016/j.geomorph.2006.10.020
771 Nejadi, S., Trivedi, J. J., & Leung, J. (2017). History matching and uncertainty quantification of
772   discrete fracture network models in fractured reservoirs. *Journal of Petroleum Science*
773   *and Engineering*, 152, 21-32. https://doi.org/10.1016/j.petrol.2017.01.048
774 Okoroafor, E. R., Co, C., & Horne, R. N. (2022). Numerical investigation of the impact of
775   fracture aperture anisotropy on EGS thermal performance. *Geothermics*, 100,
776   102354. https://doi.org/10.1016/j.geothermics.2022.102354
777 Remy, N., Boucher, A., & Wu, J. (2009). Applied geostatistics with SGeMS: A user's guide.
778   Cambridge University Press, Cambridge, U. K.
779 Romary, T. (2009). Integrating production data under uncertainty by parallel interacting Markov
780   chains on a reduced dimensional space. *Computational Geosciences*, 13, 103-122.
781   https://doi.org/10.1007/s10596-008-9108-8
782 Sarma, P., Durlofsky, L. J., & Aziz, K. (2008). Kernel principal component analysis for efficient
783   differentiable parameterization of multipoint geostatistics. *Mathematical Geosciences*,
784   40, 3–32. https://doi.org/10.1007/s11004-007-9131-7
785 Settgast, R. R., Fu, P., Walsh, S. D. C., White, J. A., Annavarapu, C., & Ryerson, F. J. (2017). A
786   fully coupled method for massively parallel simulation of hydraulically driven fractures

787   in 3-dimensions. *International Journal for Numerical and Analytical Methods in*
788   *Geomechanics*, 41, 627–653. https://doi.org/10.1002/nag.2557

789 Shi, Z., Zhang, S., Yan, R., & Wang, G. (2018). Fault zone permeability decrease following
790   large earthquakes in a hydrothermal system. *Geophysical Research Letters*, 45, 1387-
791   1394. https://doi.org/10.1002/2017GL075821

792 Somogyvári, Y., Jalali, M., Jimenez Parras, S., Bayer, P. (2017). Synthetic fracture network
793   characterization with transdimensional inversion. *Water Resources Research*, *53*(*6*),
794   5104-5123. https://doi.org/10.1002/2016WR020293

795 Strebelle, S. (2002). Conditional simulation of complex geological structures using multiple-
796   point statistics. *Mathematical geology*, 34(1), 1-21.
797   https://doi.org/10.1023/A:1014009426274

798 Tang, H., Fu, P., Sherman, C. S., Zhang, J., Ju, X., Hamon, F., et al. (2021). A deep learning-
799   accelerated data assimilation and forecasting workflow for commercial-scale geologic
800   carbon storage. *International Journal of Greenhouse Gas Control*, 112, 103488.
801   https://doi.org/10.1016/j.ijggc.2021.103488

802 Vo, H. X., & Durlofsky, L. J. (2014). A new differentiable parameterization based on principal
803   component analysis for the low-dimensional rep- resentation of complex geological
804   models. *Mathematical Geosciences*, 46(7), 775-813. https://doi.org/10.1007/s11004-014-
805   9541-2

806 Vogler, D., Settgast, R. R., Annavarapu, C., Madonna, C., Bayer, P., & Amann, F. (2018).
807   Experiments and simulations of fully hydro-mechanically coupled response of rough
808   fractures exposed to high-pressure fluid injection. *Journal of Geophysical Research:*
809   *Solid Earth*, 123, 1186-1200. https://doi.org/10.1002/2017JB015057

810 Vogt, C., Marquart, G., Kosack, C., Wolf, A., & Clauser, C. (2012). Estimating the permeability
811   distribution and its uncertainty at the EGS demonstration reservoir Soultz-sous-Forêts
812   using the ensemble Kalman filter. *Water Resources Research*, 48, W08517. https://doi.
813   org/10.1029/2011WR011673

814 Wu, H., Fu, P., Morris, J. P., Mattson, E. D., Neupane, G., Smith, M. M., et al., & EGS. (2021).
815   Characterization of flow and transport in a fracture network at the EGS Collab field
816   experiment through stochastic modeling of tracer recovery. *Journal of Hydrology*, 593,
817   125888. https://doi. org/10.1016/j.jhydrol.2020.125888

818 Wu, H., Fu, P., Hawkins, A. J., Tang, H., & Morris, J. P. (2021). Predicting thermal performance
819   of an enhanced geothermal system from tracer tests in a data assimilation framework.
820   *Water Resources Research*, 57, e2021WR030987.
821   https://doi.org/10.1029/2021WR030987

822 Wu, H., Fu, P., Yang, X., Morris, J. P., Johnson, T. C., Settgast, R. R., & Ryerson, F. J. (2019).
823   Accurate imaging of hydraulic fractures using templated electrical resistivity
824   tomography. *Geothermics*, 81, 74-87. https://doi.org/10.1016/j.geothermics.2019.04.004

825 Xiao, C., & Tian, L. (2020). Surrogate-based joint estimation of subsurface geological and
826   relative permeability parameters for high-dimensional inverse problem by use of smooth
827   local parameterization. *Water Resources Research*, 56, e2019WR025366. https://doi.org/
828   10.1029/2019WR025366

829 Xiao, C., Zhang, S., Ma, X., Jin, J., & Zhou, T. (2022). Model-reduced adjoint-based inversion
830   using deep- learning: Example of geological carbon sequestration modeling. *Water*
831   *Resources Research*, 58, e2021WR031041. https://doi.org/10.1029/2021WR031041

832   Yang, H., Lin, Y., Wohlberg, B., & Tartakovsky, D. M. (2021). Consensus equilibrium for
833   subsurface delineation. *Water Resources Research*, 57(10), e2021WR030151.
834   https://doi.org/10.1029/2021WR030151

835   Zhang, J., Zheng, Q., Chen, D., Wu, L., & Zeng, L. (2020). Surrogate-based bayesian inverse
836   modeling of the hydrological system: An adaptive approach considering surrogate
837   approximation error. *Water Resources Research*, 56, e2019WR025721. https://
838   doi.org/10.1029/2019WR025721

839   Zhao, Y., & Luo, J. (2020). Reformulation of Bayesian geostatistical approach on principal
840   components. *Water Resources Research*, 55, e2019WR026732. https://doi.org/
841   10.1029/2019WR026732

842   Zhu, Y., & Zabaras, N. (2018). Bayesian deep convolutional encoder-decoder networks for
843   surrogate modeling and uncertainty quantification. *Journal of Computational Physics*,
844   366, 415-447. https://doi.org/10.1016/j.jcp.2018.04.018